Journal of Molecular Spectroscopy 332 (2017) 16–21

Contents lists available at ScienceDirect

Journal of Molecular Spectroscopy

journal homepage: www.elsevier.com/locate/jms

High-resolution photoelectron imaging of cryogenically cooled α- and β-furanyl anions

Jessalyn A. DeVine [a], Marissa L. Weichman [a], Steven J. Lyle [a], Daniel M. Neumark [a,b,*]

[a] Department of Chemistry, University of California, Berkeley, CA 94720, United States
[b] Chemical Sciences Division, Lawrence Berkeley National Laboratory, Berkeley, CA 94720, USA

ARTICLE INFO

Article history:
Received 4 July 2016
In revised form 26 August 2016
Accepted 6 September 2016
Available online 9 September 2016

Keywords:
Photoelectron spectroscopy
Velocity-map imaging
Aromatic heterocycle
Radical
Furan

ABSTRACT

Isomer-specific, high-resolution photoelectron spectra of α- and β-furanyl obtained *via* slow electron velocity-map imaging of cryogenically cooled anions are reported. The spectra yield electron affinities of 1.8546(4) and 1.6566(4) eV for the α- and β-furanyl neutral radicals, respectively. New vibronic structure is resolved and assigned based on density functional theory and Franck-Condon simulations, providing several vibrational frequencies for the ground electronic state of both neutral isomers. Subtle differences in orbital hybridization resulting from varying proximity of the deprotonated carbon to the heteroatom are inferred from photoelectron angular distributions, and the C_β—H bond dissociation energy is estimated from a combination of experimental and theoretical results to be 119.9(2) kcal mol^{-1}.

1. Introduction

Furan (C_4H_4O) is a well-known aromatic heterocycle that plays a role in many chemical processes and applications. Substituted furans are widely used to construct intermediates in organic synthesis, providing a valuable route to the formation of carbon-carbon bonds [1]. A primary structural component of coal [2], the high energy density of furan and its facile production from biomass have led to the use of furanic compounds as components of biofuel [3–5]. Central to the large-scale use of furan-based biofuels is an understanding of the thermochemistry of furan, and the major product channels of its thermal decomposition have been identified using flow reactors and reflected shock tubes [6–8]. Several proposed mechanisms for the pyrolysis of furan indicate formation of the furanyl radicals (Fig. 1) through the reaction of furan with the primary products of its decomposition [9–12]; thus, characterization of these intrinsically reactive species could be of interest in further understanding the chemical processes involved in the combustion of furan-containing biofuels.

Characterization of the furanyl radicals has largely been accomplished through photoelectron spectroscopy (PES) of furanyl anions formed from nonspecific deprotonation of furan [13,14]. Due to the relative acidity of the α-carbon in furan and the consequent stability of the corresponding anion [15], these experiments have been limited to the α-furanyl system. In this work, we obtain high resolution PE spectra of both the α- and β-furanyl radicals by slow electron velocity-map imaging of cryogenically-cooled furanyl anions (cryo-SEVI).

The photoelectron spectrum of the α-furanyl anion was first reported by Vogelhuber and coworkers [13], providing the adiabatic electron affinity (EA) for neutral α-furanyl, three vibrational frequencies for its radical $\tilde{X}^2A'$ ground state, and the term energy for the $\tilde{A}^2A''$ excited state. This study also provided the first experimentally-derived measure of the C_α—H bond dissociation enthalpy (BDE) of furan, giving a value of 119.9(2) kcal mol^{-1}. Photoelectron imaging experiments carried out by the Sanov group have provided the term energy for the $\tilde{B}^2A''$ excited state of the α-furanyl radical, and comparison of the photoelectron angular distributions for this system and other aromatic heterocycles highlighted a connection between orbital hybridization and aromatic stabilization, with more fractional *p*-character in the highest-occupied molecular orbital (HOMO) of the anion corresponding to a greater degree of aromatic stabilization in the protonated parent molecule [14,16]. In all of these experiments, negligible contribution from the β-furanyl anion was observed, reflecting the relative stability of the α-furanyl anion.

Slow electron velocity-map imaging (SEVI) of negative ions is a variant of traditional PES which employs a velocity-map imaging (VMI) detection scheme and a tunable detachment laser to selectively detect slow photoelectrons in high resolution, thus providing

* Corresponding author at: Chemical Sciences Division, Lawrence Berkeley National Laboratory, Berkeley, CA 94720, USA.
E-mail address: dneumark@berkeley.edu (D.M. Neumark).

http://dx.doi.org/10.1016/j.jms.2016.09.002
0022-2852/

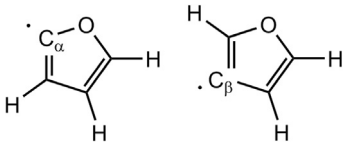

Fig. 1. Molecular structures of (left) α- and (right) β-furanyl radicals.

a detailed probe of electronic and vibrational energies of the neutral species generated upon photodetachment [17]. Incorporation of a cryogenically-cooled ion trap into the SEVI apparatus results in efficient cooling of the anion internal degrees of freedom, reducing spectral congestion and providing narrow (2–4 cm^{-1}) spectral features [18]. Cryo-SEVI has been extremely successful in characterizing the vibronic structure of radicals with sub-meV resolution [19–21], and the use of trimethylsilyl (TMS) substituted molecular precursors has provided isomer-specific photoelectron spectra for systems such as the anthracenyl and naphthyl radicals [22,23].

We present isomer-specific cryo-SEVI spectra of the two furanyl anions, and report electron affinities and ground-state vibrational frequencies for the corresponding radicals. This work is the first spectroscopic investigation of the β-furanyl neutral and anion, using an appropriate TMS-based precursor to generate the anion, and represents a considerable improvement in resolution upon the previously published α-furanyl spectra from the Lineberger and Sanov groups [13,14,16]. Additionally, the angular information provided by cryo-SEVI is used to discuss differences in orbital hybridization resulting from proximity of the heteroatom to the deprotonated carbon, and the C_β—H bond energy of furan is estimated.

2. Methods

2.1. Experimental

The cryo-SEVI method and apparatus have been described in detail previously [17,24,25]. Briefly, anions are cryogenically cooled, mass-selected, and photodetached with a tunable laser. The photoelectron velocity distribution is measured using a VMI spectrometer operating at relatively low extraction voltages, providing enhanced resolution for the slowest electrons. Our current configuration includes a recently redesigned VMI lens, which is capable of resolving peaks as narrow as 1.2 cm^{-1} for detachment from atomic anions [23].

The furanyl anions were formed by supersonic expansion of a neutral molecular precursor and trace NF_3 in helium through an Even-Lavie pulsed molecular beam valve fitted with a circular filament ionizer [26]. Injection of electrons from the ionizer resulted in dissociative electron attachment to NF_3, forming fluoride anions which then reacted with the molecular precursor to produce the desired anions. Use of furan as a precursor largely produced the α-furanyl anion, with little to no contribution from the β-isomer. To obtain the β-furanyl anion, the NF_3/He mixture was passed through a cartridge containing 3-(trimethylsilyl)furan held at 70 °C, which reacted with F^- to selectively form the β-furanyl anion due to the strength of the fluorine-silicon bond [27]. Details of the synthesis of 3-(trimethylsilyl)furan are provided in the supplementary information.

Ions were then passed through a radiofrequency (rf) hexapole ion guide and quadrupole mass filter, and directed into a linear rf octupole ion trap. The ions were confined in the trap for around 40 ms, where collisions with a 20:80 H_2:He buffer gas mixture held at 5 K resulted in relaxation to their ground vibrational state; typical internal temperatures of 10 K are obtained following this cooling period for molecular systems [18]. The ions were then extracted into an orthogonal Wiley-McLaren time-of-flight mass spectrometer [28] and focused into the interaction region of a VMI electrostatic lens [29], where they were photodetached by the output of a Nd:YAG-pumped tunable dye laser. The resultant photoelectrons were imaged on a position-sensitive detector comprised of two chevron-stacked microchannel plates coupled to a phosphor screen, which was photographed by a CCD camera with each laser shot [30].

Event-counting software was used to identify single electron events in each photograph, binning the centroid of each event [31]. This was repeated over tens of thousands of laser shots, and the maximum-entropy velocity Lengendre reconstruction method was used to extract the radial and angular distributions from the accumulated images [32]. Radial distance was related to velocity, and thus electron kinetic energy (eKE), by calibration with the well-characterized detachment transitions of atomic O^- [33]. Because eKE changes with photon energy, spectra are reported as a function of electron binding energy (eBE), given by eBE = $h\nu$ − eKE.

2.2. Theoretical

To assist in spectral assignments, geometry optimizations and frequency calculations were carried out for the anion and neutral ground state of α- and β-furanyl at the B3LYP/6-311+G* level in Gaussian 09 [34]. Optimized geometries, relative energies, and harmonic frequencies are provided in Tables S1–4 of the supplementary information.

The DFT geometries, frequencies, and normal mode coordinates were then used to simulate the Franck-Condon (FC) profile for detachment from the two anion isomers. The Duschinsky transformation [35],

$$\mathbf{Q} = \mathbf{J}\mathbf{Q}' + \mathbf{K} \quad (1)$$

was used to relate the neutral ($\mathbf{Q}'$) and anion ($\mathbf{Q}$) coordinates, where $\mathbf{J}$ is the block-diagonal Duschinsky rotation matrix and $\mathbf{K}$ expresses the difference in anion and neutral geometries in terms of the anion normal coordinates. The $\mathbf{J}$ and $\mathbf{K}$ matrices were computed using FCFGAUSS [36], and PESCAL [37] took these as inputs to calculate Franck-Condon intensities using the Sharp and Rosenstock [38] method with corrections by Chen [39]. DFT harmonic frequencies were scaled to match the experimental frequencies, with scaling factors ranging from 0.975 to 0.999.

Absolute gas-phase enthalpies of the two anion isomers were obtained using the implementation of the Weizmann-1 theory in Gaussian 09 [40], replacing the coupled cluster calculations with Bruenecker doubles to obtain the most accurate energies [41]. Calculated enthalpies are reported in Table S6 of the supplementary material, and correspond to the total electronic energy of the species plus a thermal correction for a temperature of 273.15 K.

3. Results

The cryo-SEVI spectra of the α- and β-furanyl anions are presented in Fig. 2. As in previous work [19,20,22,23], the blue traces correspond to an overview spectrum taken with a high photon energy, and the black traces are high-resolution SEVI scans that are taken near-threshold and scaled to match overview intensities. In the spectra of both species, peak A corresponds to the vibrational origin of the $\tilde{X}^2A' \leftarrow \tilde{X}^1A'$ transition, yielding adiabatic electron affinities of 1.8546(4) and 1.6566(4) eV for the α- and β-furanyl radicals, respectively. Assignments of spectral features to vibrational transitions are presented in Tables 1 and 2, permitting extraction of several vibrational frequencies of the neutral radicals.

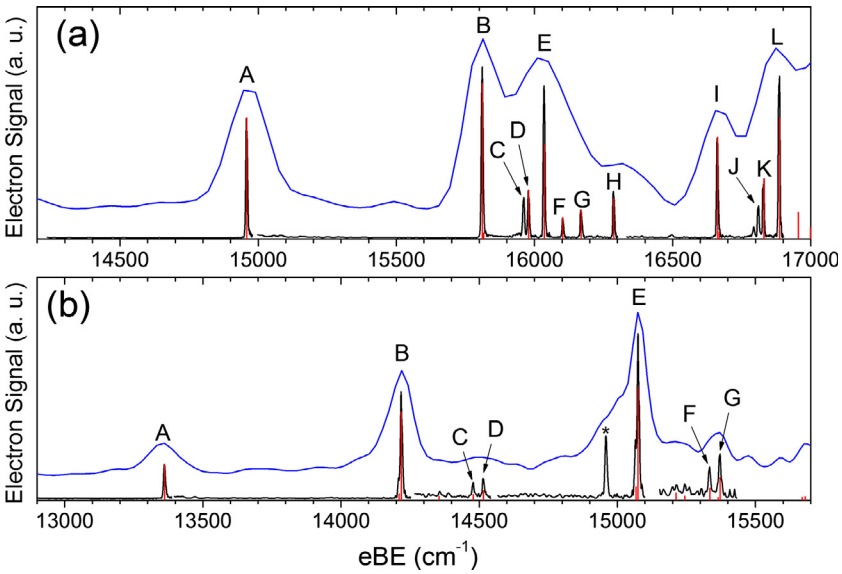

Fig. 2. SEVI spectra of the (a) α- and (b) β-furanyl anions. The blue traces are low-resolution overview scans, and the black traces are high-resolution scans taken near-threshold and scaled to match the overview intensities. The stick spectrum represents results of FC simulations (red). (For interpretation of the references to color in this figure legend, the reader is referred to the web version of this article.)

Table 1
Peak positions (cm^{-1}), shifts from the origin (cm^{-1}), and vibrational assignments for features observed in the $\tilde{X}^2A' \leftarrow \tilde{X}^1A'$ detachment transition of the α-furanyl anion. All peaks had a Gaussian full-width at half-maximum of 7–8 cm^{-1}.

Peak	eBE	Shift	Assn.
A	14,958	0	0_0^0
B	15,810	852	13_0^1
C	15,961	1002	11_0^1
D	15,978	1020	10_0^1
E	16,035	1076	9_0^1
F	16,102	1144	8_0^1
G	16,169	1210	7_0^1
H	16,286	1328	6_0^1
I	16,662	1703	13_0^2
J	16,810	1852	$11_0^1 13_0^1$
K	16,828	1870	$10_0^1 13_0^1$
L	16,885	1927	$9_0^1 13_0^1$

Table 2
Peak positions (cm^{-1}), shifts from the origin (cm^{-1}), and vibrational assignments for features observed in the $\tilde{X}^2A' \leftarrow \tilde{X}^1A'$ detachment transition of the β-furanyl anion. All peaks had a Gaussian full-width at half-maximum of 8–9 cm^{-1}.

Peak	eBE	Shift	Assn.
A	13,361	0	0_0^0
B	14,218	857	12_0^1
C	14,478	1117	9_0^1
D	14,515	1154	8_0^1
E	15,075	1714	12_0^2
F	15,333	1972	$9_0^1 12_0^1$
G	15,371	2010	$8_0^1 12_0^1$

Our DFT calculations indicate that the α-furanyl anion is ~0.2 eV more stable than the β-isomer, whereas the neutrals are within 20 meV of each other; thus, the 0.2 eV difference in EAs for the two radicals is largely a reflection of the relative stability of the α-furanyl anion. This stability also led to some contamination from the α-isomer in the spectrum of the β-furanyl anion; the intensity of the α-furanyl vibrational origin (indicated by an asterisk in Fig. 2b) relative to features in the β-furanyl spectrum was found to be dependent on the amount of buffer gas used to cool the ions, suggesting that the ions isomerize with H_2 in the octupole trap.

In addition to transition energies, SEVI yields the photoelectron angular distribution (PAD) associated with a particular photodetachment transition. For detachment with a single linearly polarized photon, the PAD is given by [42]

$$\frac{d\sigma}{d\Omega} = \frac{\sigma_{tot}}{4\pi}[1 + \beta P_2(\cos\theta)] \quad (2)$$

where σ_{tot} is the total detachment cross section, $P_2(x)$ is the second-order Legendre polynomial, θ is the angle of the outgoing electron's velocity vector with respect to the laser polarization axis, and β is the anisotropy parameter, which ranges from −1 to +2 corresponding to perpendicular and parallel detachment, respectively. The anisotropy parameter reflects the symmetry and angular momentum of the orbital from which an electron is detached; detachment from *s*-like orbitals results in outgoing *p*-wave electrons and parallel PADs ($\beta > 0$), whereas detachment from *p*-like orbitals results in outgoing *s*- and *d*-wave electrons, generally yielding isotropic PADs ($\beta = 0$) or PADs with $\beta < 0$ [43].

The PADs of α- and β-furanyl are presented in Fig. 3. Both isomers show negative anisotropies, though the energy dependence of β is distinctly different between the two, with the β-isomer displaying more perpendicular PADs for moderate kinetic energies. This suggests a difference in the orbital hybridization between the two isomers, which will be discussed in detail in the following section.

4. Discussion

4.1. Spectral assignments

The FC simulations for both isomers show generally excellent agreement with experiment, providing straightforward assignment of most observed vibronic features and yielding several vibrational frequencies, summarized in Table 3. As furanyl has C_s symmetry, the FC-allowed vibrational transitions all correspond to totally symmetric in-plane motions of the neutral radical, shown in Fig. 4. The most significant geometry change upon photodetach-

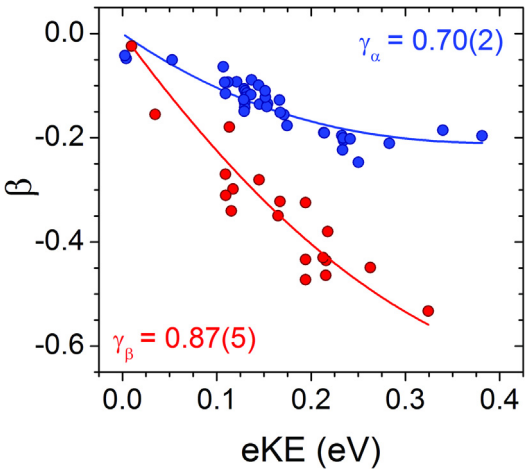

Fig. 3. Experimental PADs and fits of the anisotropy parameters to the mixed *s-p* model (Eq. (2)) for (blue) α- and (red) β-furanyl. Errors correspond to one standard deviation from the regression results. (For interpretation of the references to color in this figure legend, the reader is referred to the web version of this article.)

Table 3
Experimental and calculated electron affinities and vibrational frequencies for the $\tilde{X}^2A'$ state of α- and β-furanyl. Uncertainties represent one standard deviation of a Gaussian fit to the experimental peak.

	Exp.	Calc.
α		
EA, eV	1.8546 (4)	1.8429
υ_6, cm^{-1}	1328 (4)	1362
υ_7, cm^{-1}	1210 (5)	1235
υ_8, cm^{-1}	1144 (4)	1170
υ_9, cm^{-1}	1076 (4)	1095
υ_{10}, cm^{-1}	1020 (4)	1022
υ_{11}, cm^{-1}	1002 (4)	1003
υ_{13}, cm^{-1}	852 (4)	868
β		
EA, eV	1.6566 (4)	1.6404
υ_8, cm^{-1}	1154 (5)	1174
υ_9, cm^{-1}	1117 (5)	1138
υ_{12}, cm^{-1}	857 (5)	867

ment from the furanyl anion is an increase in the ring-angle centered on the deprotonated carbon due to removal of electron density from the lone pair orbital (Fig. 5); as such, the most FC-active mode in both isomers (υ_{13} in α-furanyl, υ_{12} in β-furanyl) involves a large distortion of this angle. Of the seven frequencies obtained for the α-isomer, only three (υ_6, υ_9, and υ_{13}) have been previously measured experimentally [13].

Peaks C and J are absent in the FC simulation for α-furanyl based on the DFT geometries, so their assignment requires further consideration. Each of these peaks lies ~20 cm^{-1} below a transition involving υ_{10} (10_0^1 for C and $10_0^1 13_0^1$ for J); due to the ~19 cm^{-1} difference in the DFT harmonic frequencies for υ_{10} and υ_{11}, we assign peaks C and J to the 11_0^1 and $11_0^1 13_0^1$ transitions, respectively. Modest changes in normal mode displacements, corresponding to changes in the neutral geometry relative to the anion, may result in increased FC-activity of υ_{11}. The geometry displacement along υ_{11} was allowed to vary using the optimization feature of PESCAL, and this was found to result in the appearance of peaks C and J with appropriate intensity in the simulated spectrum, shown in Fig. S2 of the supplementary material. The corresponding difference between the DFT and optimized geometry has a norm of 0.086 Å, and the most significant geometry changes are a 0.019 Å decrease in the C_β—C_β bond length and a 0.019 Å increase in the distance

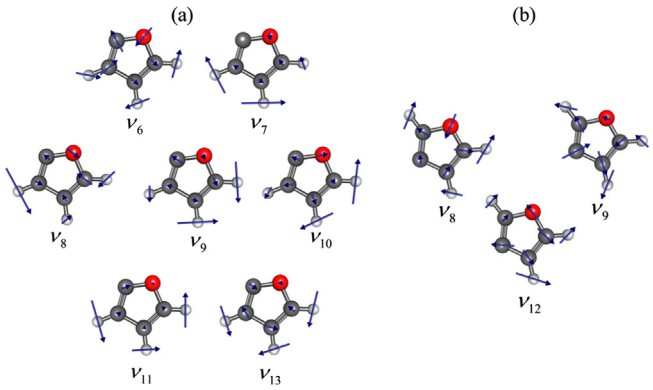

Fig. 4. Normal modes for the (a) α- and (b) β-furanyl radicals.

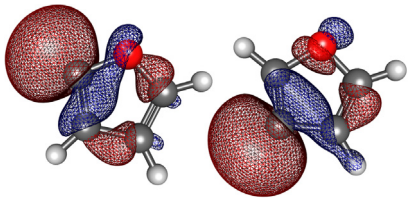

Fig. 5. Highest-occupied molecular orbitals for the (left) α- and (right) β-furanyl anions.

between the oxygen and the protonated α-carbon. A summary of the geometry changes is presented in Table S5 of the supporting information. The small changes required to fit the spectrum suggest that the absence of peaks C and J from the DFT-based FC simulations is indeed due to slight inaccuracies in the calculated geometry changes that occur upon photodetachment of the α-furanyl anion.

4.2. Photoelectron angular distributions

As can be seen in Fig. 3, the anisotropy parameters for the two furanyl isomers show distinct energy dependences. The HOMO of the furanyl anion is nominally sp^2 hybridized and primarily localized on a single carbon atom (Fig. 5). Thus, to more quantitatively analyze the PADs provided by SEVI, we will employ the single-center mixed *s-p* model developed by Sanov and coworkers, which they successfully applied to the α-furanyl anion [14,16]. Previously, cryo-SEVI has been used to identify isomeric trends in the PADs of polycyclic aromatic hydrocarbons [22,23]; in a similar vein, we presently aim to use the isomer-specificity of our furanyl spectra to compare orbital hybridization for radical heterocycles with varying proximity between the radical carbon and the heteroatom.

In the mixed *s-p* model, the orbital from which an electron is detached is taken to be a single-center orbital comprised of *s*- and *p*-components, with fractional *p*-character γ. Since low kinetic energies (<0.5 eV) are considered in this work, the relative scaling of the possible detachment channels is given by the Wigner threshold law [44], permitting replacement of the radial dipole integrals in the Cooper-Zare formula with the *A* and *B* Hanstorp coefficients [45]. As was shown by Sanov and coworkers, the anisotropy of the mixed *s-p* model orbital can then be expressed as

$$\beta(\mathrm{eKE}) = \frac{2\left[\frac{B}{A}\left(\frac{1-\gamma}{\gamma}\right) - 2\right]A\cdot\mathrm{eKE} + 2(A\cdot\mathrm{eKE})^2}{1 + \frac{B}{A}\left(\frac{1-\gamma}{\gamma}\right)A\cdot\mathrm{eKE} + 2(A\cdot\mathrm{eKE})^2} \quad (3)$$

where A reflects the relative scaling of the $p \rightarrow d$ and $p \rightarrow s$ detachment channels, and B represents the relative scaling of the $p \rightarrow s$ and $s \rightarrow p$ detachment channels [46].

As was done in the treatment of the α-furanyl anion by Culberson and coworkers, we will take B/A to be 8/3, which has been successful in describing detachment from mixed $2s$–$2p$ orbitals [47]. Due to the relatively localized nature of the anion orbital on the deprotonated carbon, we will use $A = 0.75\ eV^{-1}$, which corresponds to detachment from atomic C^- and has been used previously to describe the PADs of aromatic radicals [48,49]. Thus we obtain a single-parameter expression for $\beta(eKE)$, which can be fit to the experimental PADs to extract γ for both isomers. We obtain values of 0.70 and 0.87 for α- and β-furanyl, respectively, demonstrating that the β-furanyl anion has more fractional p-character. This is consistent with the trends in PADs of deprotonated aromatic heterocycles, where less fractional p-character was observed for anions with closer proximity between the site of deprotonation and electron-withdrawing heteroatoms [16]. This proximity effect may also account for the higher electron affinity of the α-isomer, given that the anion HOMO for this isomer is more delocalized onto the heteroatom than in the β-isomer (see Fig. 5).

4.3. C_β—H bond dissociation energy of furan

The thermochemistry of furan has attracted considerable attention, in part due to its unusually strong C—H bonds [50]. Using a standard gas-phase acidity/electron affinity thermodynamic cycle (elaborated in the supplementary material), the C—H bond dissociation enthalpy (BDE) is given by

$$\mathrm{BDE(R{-}H)} = \Delta H^\circ_{acid}(\mathrm{RH}) + \mathrm{EA(R^-)} - \mathrm{IE(H)} \quad (4)$$

where $\Delta H^\circ_{acid}(RH)$ is the gas-phase acidity of RH, $EA(R^-)$ is the electron affinity of the deprotonated neutral, and IE(H) is the ionization energy of hydrogen, which is well-known to be 313.6 kcal mol^{-1} [51]. Previously, using experimental values of the gas-phase acidity and electron affinity of α-furanyl, this equation was used to calculate the C_α—H BDE of furan, giving a value of 119.8(2) kcal mol^{-1} [13]. Our measurement of the EA of β-furanyl motivates a similar calculation to obtain the C_β—H BDE of furan, but experimental gas-phase acidity data for the β-position of furan is not available, and previous theoretical calculations were not carried out at a very high level [15]. To estimate the C_β—H BDE, we will take an approach similar to that used in the estimation of the C_2—H BDE in oxazole [16]; specifically, we determine from *ab initio* calculations the expected difference in gas-phase acidities for the α- and β-positions of furan, and use this difference with the experimentally determined gas-phase acidity for the α-carbon to yield a hybrid experimental-theoretical estimation of the gas-phase acidity of the β-carbon in furan. This will then be used with our experimental EA for β-furanyl to determine the C_β—H BDE of furan.

In terms of the absolute enthalpies, the gas-phase acidity for the α/β-carbon of furan is given by

$$\Delta H^\circ_{acid}(\alpha/\beta) = H^\circ(\alpha/\beta - C_4H_3O^-) + H^\circ(H) - H^\circ(\mathrm{furan}) \quad (5)$$

Evidently, the difference in gas phase acidities is simply the difference in the absolute enthalpies of the anion isomers. From the enthalpies in Table S6 of the supplementary material, we find that the α-carbon of furan is around 4.6 kcal mol^{-1} more acidic; using the gas-phase acidity reported by Grabowski and coworkers ($\Delta H^\circ_{acid}(\alpha) = 390.7 \pm 0.2$ kcal mol^{-1}) [52], this gives an estimate of $\Delta H^\circ_{acid}(\beta) = 395.3(2)$ kcal mol^{-1}. Substituting this into equation (4), we obtain the experimental-theoretical BDE of the C_β—H bond of furan to be 119.9(2) kcal mol^{-1}; our calculations indicate that the C_β—H bond is only stronger than the C_α—H bond by 0.05 kcal mol^{-1}, which is smaller than the uncertainty imposed by the experimental determination of $\Delta H^\circ_{acid}(\alpha)$. This result is consistent with our earlier assertion that the differences in electron affinities between the two isomers is only a reflection of the energetic ordering of the anions, and that the radical isomers are equally stable. Additionally, the estimated gas-phase acidity explains the lack of formation of the β-furanyl anion from reaction of furan with fluoride anions that has prevented prior experimental observation of this isomer.

5. Conclusion

High-resolution photoelectron spectra of the cryo-cooled α- and β-furanyl anions have been obtained using slow photoelectron velocity-map imaging. In the case of the α-furanyl system, an order-of-magnitude improvement in resolution over previous PES investigations is achieved, resulting in newly resolved vibronic structure that permits extraction and refinement of several vibrational frequencies. The β-furanyl anion has been probed experimentally for the first time, providing its electron affinity, several vibrational frequencies, and an experimental-theoretical estimation of the C_β—H bond dissociation enthalpy of furan. The photoelectron angular distributions for the two isomers reflect differences in orbital hybridization that are related to the proximity of the site of deprotonation to the heteroatom, and these are used to explain the energetic ordering of the furanyl anions.

Acknowledgments

This research is funded by the Director, Office of Basic Energy Sciences, Chemical Sciences Division of the US Department of Energy under Contract DE-AC02-05CH11231. M.L.W. thanks the National Science Foundation for a graduate research fellowship.

Appendix A. Supplementary material

Supplementary data associated with this article can be found, in the online version, at http://dx.doi.org/10.1016/j.jms.2016.09.002.

References

[1] B.H. Lipshutz, Chem. Rev. 86 (1986) 795.
[2] K.L. Smith, L.D. Smoot, T.H. Fletcher, R.J. Pugmire, The Plenum Chemical Engineering Series. The Structure and Reaction Processes of Coal, vol. 4, Springer, 1994.
[3] M. Mascal, E.B. Nikitin, Angew. Chem. Int. Ed. 47 (2008) 7924.
[4] J.P. Lange, E. van der Heide, J. van Buijtenen, R. Price, Chem. Sus. Chem. 5 (2012) 150.
[5] M.S. Mettler, S.H. Mushrif, A.D. Paulsen, A.D. Javadekar, D.G. Vlachos, P.J. Dauenhauer, Energy Environ. Sci. 5 (2012) 5414.
[6] O.S.L. Bruinsma, P.J.J. Tromp, H.J.J.D. Nolting, J.A. Moulijn, Fuel 67 (1988) 334.
[7] D. Fulle, A. Dib, J.H. Kiefer, Q. Zhang, J. Yao, R.D. Kern, J. Phys. Chem. A 102 (1998) 7480.
[8] M.A. Grela, V.T. Amorebieta, A.J. Colussi, J. Phys. Chem. 89 (1985) 38.
[9] A. Lifshitz, M. Bidani, S. Bidani, J. Phys. Chem. 90 (1986) 5373.
[10] A. Lifshitz, C. Tamburu, R. Shashua, J. Phys. Chem. A 102 (1998) 10655.
[11] P.P. Organ, J.C. Mackie, J. Chem. Soc., Faraday Trans. 87 (1991) 815.
[12] K. Sendt, G.B. Bacskay, J.C. Mackie, J. Phys. Chem. A 104 (2000) 1861.
[13] K.M. Vogelhuber, S.W. Wren, L. Sheps, W.C. Lineberger, J. Chem. Phys. 134 (2011) 064302.
[14] L.M. Culberson, A. Sanov, J. Chem. Phys. 134 (2011) 204306.
[15] C.H. Depuy, S.R. Kass, G.P. Bean, J. Org. Chem. 53 (1988) 4427.
[16] L.M. Culberson, C.C. Blackstone, A.A. Wallace, A. Sanov, J. Phys. Chem. A 119 (2015) 9770.
[17] D.M. Neumark, J. Phys. Chem. A 112 (2008) 13287.
[18] C. Hock, J.B. Kim, M.L. Weichman, T.I. Yacovitch, D.M. Neumark, J. Chem. Phys. 137 (2012) 244201.
[19] J.B. Kim, M.L. Weichman, T.I. Yacovitch, C. Shih, D.M. Neumark, J. Chem. Phys. 139 (2013) 104301.
[20] M.L. Weichman, J.B. Kim, D.M. Neumark, J. Chem. Phys. 140 (2014) 104305.
[21] M.L. Weichman, J.B. Kim, D.M. Neumark, J. Phys. Chem. A 119 (2015) 6140.
[22] M.L. Weichman, J.B. Kim, J.A. DeVine, D.S. Levine, D.M. Neumark, J. Am. Chem. Soc. 137 (2015) 1420.

[23] M.L. Weichman, J.A. DeVine, D.S. Levine, J.B. Kim, D.M. Neumark, PNAS 113 (2016) 1698.
[24] A. Osterwalder, M.J. Nee, J. Zhou, D.M. Neumark, J. Chem. Phys. 121 (2004) 6317.
[25] C. Hock, J.B. Kim, M.L. Weichman, T.I. Yacovitch, D.M. Neumark, J. Chem. Phys. 137 (2012).
[26] U. Even, J. Jortner, D. Noy, N. Lavie, C. Cossart-Magos, J. Chem. Phys. 112 (2000) 8068.
[27] C.H. Depuy, V.M. Bierbaum, L.A. Flippin, J.J. Grabowski, G.K. King, R.J. Schmitt, S.A. Sullivan, J. Am. Chem. Soc. 102 (1980) 5012.
[28] W.C. Wiley, I.H. Mclaren, Rev. Sci. Instrum. 26 (1955) 1150.
[29] A.T.J.B. Eppink, D.H. Parker, Rev. Sci. Instrum. 68 (1997) 3477.
[30] D.W. Chandler, P.L. Houston, J. Chem. Phys. 87 (1987) 1445.
[31] M.B. Doyle, C. Abeyasera, A.G. Suits, NuACQ. <http://chem.wayne.edu/suitsgroup/NuACQ.html>.
[32] B. Dick, Phys. Chem. Chem. Phys. 16 (2014) 570.
[33] C. Blondel, W. Chaibi, C. Delsart, C. Drag, F. Goldfarb, S. Kroger, Eur. Phys. J. D 33 (2005) 335.
[34] M.J. Frisch, G.W. Trucks, H.B. Schlegel, G.E. Scuseria, M.A. Robb, J.R. Cheeseman, G. Scalmani, V. Barone, B. Mennucci, G.A. Petersson, H. Nakatsuji, M. Caricato, X. Li, H.P. Hratchian, A.F. Izmaylov, J. Bloino, G. Zheng, J.L. Sonnenberg, M. Hada, M. Ehara, K. Toyota, R. Fukuda, J. Hasegawa, M. Ishida, T. Nakajima, Y. Honda, O. Kitao, H. Nakai, T. Vreven, J.A. Montgomery, J.E. Peralta, F. Ogliaro, M. Bearpark, J.J. Heyd, E. Brothers, K.N. Kudin, V.N. Staroverov, R. Kobayashi, J. Normand, K. Raghavachari, A. Rendell, J.C. Burant, S.S. Iyengar, J. Tomasi, M. Cossi, N. Rega, J.M. Millam, M. Klene, J.E. Knox, J.B. Cross, V. Bakken, C. Adamo, J. Jaramillo, R. Gomperts, R.E. Stratmann, O. Yazyev, A.J. Austin, R. Cammi, C. Pomelli, J.W. Ochterski, R.L. Martin, K. Morokuma, V.G. Zakrzewski, G.A. Voth, P. Salvador, J.J. Dannenberg, S. Dapprich, A.D. Daniels, Ö. Farkas, J.B. Foresman, J.V. Ortiz, J. Cioslowski, D.J. Fox, Gaussian 09, Revision C.01, 2009, Gaussian, Inc., Wallingford, CT. <http://www.gaussian.com>.
[35] F. Duschinsky, Acta Physicochim. URS 7 (1937) 551.
[36] K.M. Ervin, FCFGAUSS03: Gaussian 03 Output Conversion Program, 2004.
[37] K.M. Ervin, PESCAL, 2010. <http://wolfweb.unr.edu/~ervin/pes>.
[38] T.E. Sharp, H.M. Rosenstock, J. Chem. Phys. 41 (1964) 3453.
[39] P. Chen, Supersonic jets of organic radicals, in: C.Y. Ng, T. Baer, I. Powis (Eds.), Unimolecular and Bimolecular Ion-Molecule Reaction Dynamics, John Wiley, Cambridge, UK, 1994.
[40] J.M.L. Martin, G. de Oliveira, J. Chem. Phys. 111 (1999) 1843.
[41] E.C. Barnes, G.A. Petersson, J.A. Montgomery, M.J. Frisch, J.M.L. Martin, J. Chem. Theor. Comput. 5 (2009) 2687.
[42] J. Cooper, R.N. Zare, J. Chem. Phys. 48 (1968) 942.
[43] A. Sanov, Annu. Rev. Phys. Chem. 65 (2014) 341.
[44] E.P. Wigner, Phys. Rev. 73 (1948) 1002.
[45] D. Hanstorp, C. Bengtsson, D.J. Larson, Phys. Rev. A 40 (1989) 670.
[46] E.R. Grumbling, A. Sanov, J. Chem. Phys. 135 (2011) 164302.
[47] A. Sanov, E.R. Grumbling, D.J. Goebbert, L.M. Culberson, J. Chem. Phys. 138 (2013) 054311.
[48] J.L. Hall, M.W. Siegel, J. Chem. Phys. 48 (1968).
[49] L.M. Culberson, C.C. Blackstone, A. Sanov, J. Phys. Chem. A 117 (2013).
[50] J.M. Simmie, H.J. Curran, J. Phys. Chem. A 113 (2009) 5128.
[51] S.G. Lias, Ionization energy evaluation, in: P.J. Linstrom, W.G. Mallard (Eds.), NIST Chemistry WebBook, NIST Standard Reference Database, National Institute of Standards and Technology, Gaithersburg, MD, 2010.
[52] E.P. Clifford, P.G. Wenthold, W.C. Lineberger, G.B. Ellison, C.X. Wang, J.J. Grabowski, F. Vila, K.D. Jordan, J. Chem. Soc. Perk. T. 2 (1998) 1015.